

## Development in the DIII-D Tokamak of Advanced Operating Scenarios and Associated Control Techniques for ITER

M.R. Wade for the DIII-D Team

General Atomics, P.O. Box 85608, San Diego, California 92186-5608, USA

e-mail contact of main author: wade@fusion.gat.com

**Abstract.** Significant progress has been made on the DIII-D tokamak in the capability to control key plasma features and using such control to expand the operational limits of stationary and steady-state tokamak operation. Recent experiments have demonstrated the capability to suppress the key plasma instabilities of concern for ITER, including edge localized modes, neoclassical tearing modes, and resistive wall modes. In addition, the ability to regulate the rotation and current density profiles through feedback control has been demonstrated. The use of these control techniques has allowed an expansion of the envelope of viable, stationary tokamak operation, highlighted by the demonstration of sustained ( $\sim 2$  s) operation of  $\beta_N \simeq 4$  (50% above the no-wall stability limit) as well as fully noninductive operation with  $\beta \simeq 3.5\%$ . This development is supported by a vigorous basic physics program, which has provided new insights into turbulence dynamics over a large range in spatial scales, new measurements of the structure of fast-ion instabilities and their effect on the fast ion population, and important information on the transport of carbon and associated tritium co-deposition on plasma facing surfaces.

### 1. Introduction

Through the development and integration of advanced control techniques and operating scenarios, the DIII-D research program has made significant progress in its mission to develop the physics basis for the optimization of the tokamak approach to fusion energy production. In addition to demonstrating the feasibility of and developing the physics basis for individual control tools for ITER, the DIII-D Team has developed both long-pulse, inductive scenarios with normalized performance consistent with the  $Q = 10$  baseline mission of ITER and fully noninductive plasmas with normalized performance in excess of that required for the  $Q = 5$  mission in ITER [1]. These results provide additional confidence that ITER can achieve its high-level mission objectives.

This paper discusses results from DIII-D, highlighting the capabilities of these control tools, the advanced operating scenarios enabled by these tools, and key physics insight gained from experiments on DIII-D. In Sec. 2, examples of key capabilities in optimizing tokamak performance are presented including several results on high  $\beta$  instability control and internal profile control. In Sec. 3, the present status of research aimed at providing ITER with fully characterized scenarios for both its  $Q = 10$  baseline mission and  $Q = 5$  steady-state mission is discussed. Finally, in Sec. 4, examples of advances made in the basic understanding of high-temperature fusion plasmas in areas important to ITER are presented.

### 2. Plasma Control

DIII-D is equipped with a unique set of control tools that allow precise control of key aspects of plasma stability, transport, and current drive. A flexible set of non-axisymmetric coils and high-power, localized electron cyclotron current drive and heating (ECCD/ECH) provide the capability to mitigate or suppress a wide range of instabilities, including sawteeth, neoclassical tearing modes (NTMs), resistive wall modes (RWMs), and edge localized modes (ELMs). The recent reorientation of two neutral beam sources to allow co-, counter-, and balanced neutral beam injection (NBI) provides fine control of the plasma rotation, which plays a key

role in turbulence-driven transport and in certain aspects of plasma stability. The combination of excellent density control in H-mode plasmas enabled by three divertor cryopumps and the ECCD/ECH capability allows direct control of the current density profile, which is key to both the plasma stability and transport characteristics. Finally, the extensive poloidal field coil set on DIII-D allows a wide variety of plasma shapes, enabling comparative studies with other devices and detailed studies of the effect of the magnetic configuration on plasma performance. A centralized framework for effectively utilizing these control tools is provided by the DIII-D digital plasma control system (PCS), which provides a flexible environment in which to develop and implement integrated, model-based, control algorithms for these tools.

## 2.1. High $\beta$ Instability Control

Recent experiments on DIII-D have demonstrated the capability to actively suppress both NTMs and RWMs, which are predicted to limit the attainable pressure in the ITER baseline and steady-state scenarios, respectively. These control capabilities have allowed sustained operation at significantly higher  $\beta$  values than would be possible without suppression. In the best cases, the ideal stability limit is approached with  $\beta_N \approx 4$  sustained for nearly 2 s.

**Suppression of Neoclassical Tearing Modes.** The  $m=2/n=1$  NTM is expected to be the most significant instability limiting the attainable  $\beta$  in the ITER baseline ( $Q = 10$ ) scenario [1]. Previous experiments on DIII-D demonstrated the efficacy of using highly localized ECCD at the  $q = 2$  surface to stabilize the  $m=2/n=1$  NTM [2]. Recent experiments (Fig. 1) have shown that once the NTM is stabilized, the plasma pressure can be increased and then maintained at the free-boundary stability limit, provided the ECCD is applied locally to the  $q = 2$  surface. Various control algorithms have been developed and tested to maintain the ECCD deposition location optimally positioned to provide sufficient ECCD driven current in the NTM island region [3]. In Fig. 1, a “search-and-suppress” algorithm is initially used to provide the proper alignment which is then maintained using real-time tracking of  $q = 2$  surface once the NTM is suppressed by real-time equilibrium reconstructions. Using these algorithms, optimal alignment of the ECCD deposition region with the  $q = 2$  surface is maintained throughout the ECCD phase. With the NTM effectively suppressed,  $\beta_N$  is increased and maintained for  $\sim 1$  s at the no-wall, ideal stabil-

ity limit ( $\beta_N \sim 3.2$ ). About 100 ms after the ECCD is turned off at 6.5 s, a new  $m=2/n=1$  NTM is triggered, confirming the role of ECCD in the suppression of NTM. Separate experiments have demonstrated the capability to preemptively suppress the  $m=2/n=1$  NTM even as  $\beta_N$  is increased and maintained for  $\sim 1$  s at the no-wall, ideal stability limit using real-time equilibrium reconstructions for proper alignment of the ECCD

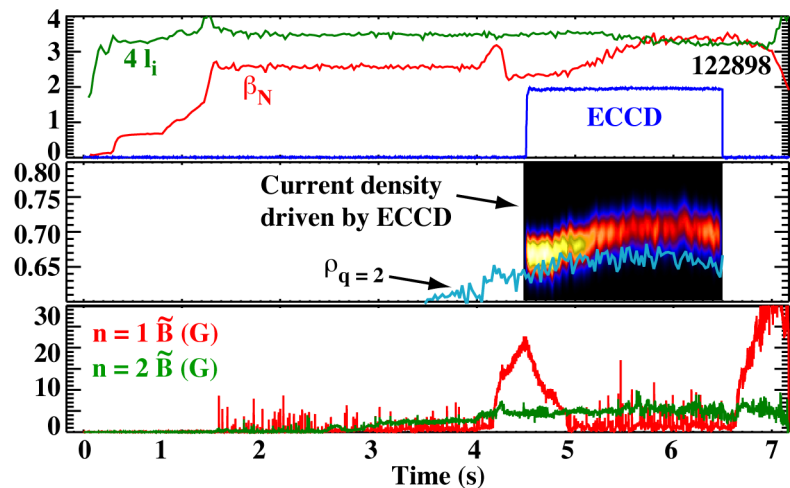


FIG. 1. Demonstration of  $m=2/n=1$  NTM suppression by ECCD, permitting operating at the no-wall  $\beta$  limit ( $\sim 4 I_i$ ). Active feedback is used to find and then maintain optimal alignment of  $J_{\text{ECCD}}(\rho)$  [image in (b)] with the location of the  $q=2$  surface (cyan).

deposition location with the  $q = 2$  surface.

### Resistive Wall Mode Stabilization.

Success in achieving the second primary physics objective of ITER – steady-state,  $Q = 5$  operation – is expected to require  $\beta$  values in excess of the no-wall  $n = 1$  stability limit  $\beta^{\text{no-wall}}$  [1]. Access to these  $\beta$  levels requires the ability to stabilize RWMs, which are destabilized as  $\beta$  is increased above  $\beta^{\text{no-wall}}$ . Using either rotational or feedback stabilization of RWMs, studies on DIII-D have demonstrated the ability to operate at pressures well above  $\beta^{\text{no-wall}}$ , in the best cases approaching the ideal-wall,  $n = 1$  stability limit  $\beta^{\text{ideal-wall}}$  [4,5]. An example of this capability is shown in Fig. 2 where RWM rotational and feedback stabilization has been

utilized to sustain  $\beta_N > 3.8$  for over 2 s [6]. In this case, the achieved  $\beta$  is approximately 50% above the conventional no-wall  $\beta$  limit ( $\sim 4 I_i$ ). Stability calculations indicate that the ideal wall stability limit in this case is  $\beta_N > 5$ , suggesting the possibility of very high  $\beta$  operation.

Previous studies on DIII-D suggested that plasma rotation is highly effective in stabilizing RWMs, provided a moderate rotation velocity (typically 1-2% of the Alfvén velocity) is maintained at the  $q = 2$  surface [4]. This threshold velocity was determined in experiments in which magnetic braking was utilized to reduce the plasma rotation. Measurements of this threshold in recent experiments in which variations in neutral beam injection (NBI) torque were used to control the rotation suggests that the threshold for rotational stabilization is considerably lower. The ability to operate above  $\beta^{\text{no-wall}}$  for  $\sim 1$  s at very low rotation values is exemplified in Fig. 3, where rotation values in the outer part of the plasma remain below 0.5% of the Alfvén velocity for more than 1 s. The stable rotation profile [Fig. 3(d)] is well below the rotation profile where the RWM was encountered in a similar discharge with magnetic braking. While a complete understanding of the differences in the observed rotational threshold for stabilization is still in progress, data suggests that the nonlinear interaction between the plasma rotation and resonant amplification of the fields used for magnetic braking may be responsible for the higher threshold previously seen with magnetic braking.

## 2.2. ELM suppression

A potential solution to ELM control on ITER has emerged from experiments on DIII-D which utilize edge resonant magnetic perturbations (RMPs) with  $n = 3$  symmetry to completely eliminate ELMs [7]. Recent experiments have extended this capability to include complete ELM suppression in a plasma shape similar to the ITER baseline shape and at a pedestal collisionality comparable to that anticipated in ITER [8]. This capability is shown in Fig. 4. The application of an  $n = 3$  RMP at 2.0 s results in the immediate elimination of ELMs even as good confinement and moderate  $\beta$  operation are maintained. The ability to

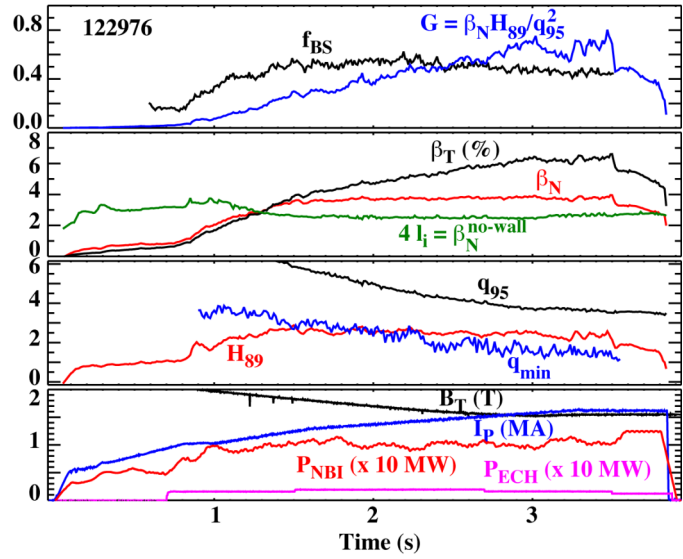


FIG. 2. Temporal evolution of a discharge with  $\beta_N > 3.8$  sustained for over 2 s. Simultaneous  $B_T$  and  $I_p$  ramps along with off-axis ECCD to form and maintain a broad current density profile.

suppress ELMs reliably has been found to be sensitive to plasma shape and  $q_{95}$  and systematically improves with lower collisionality, higher input power, and larger  $n = 3$  RMP amplitude [8]. Transport and stability analysis has shown that the observed ELM suppression results from changes in edge particle transport such that the pedestal pressure operational point can be controlled with the  $n = 3$  RMP and set slightly below the peeling-ballooning stability limit [9].

### 2.3. Disruption Mitigation

While stabilization of the instabilities mentioned above will reduce the number of disruptions in ITER, some unplanned plasma terminations will likely still occur, requiring a robust system for mitigating the effects of such a disruption. Massive gas injection (MGI) has been shown to reduce the impact of excessive thermal loads, halo currents, and runaway electron generation resulting from unmitigated plasma disruptions [10]. The DIII-D team is now developing the physics basis of this technique for extrapolation to ITER. Recent studies suggest that the transport of the impurities introduced by MGI is a multi-stage process in which MHD mixing of the impurities is an essential component [11]. These studies have shown conclusively that the injected impurities are ionized very near the plasma surface, consistent with the expectations of theory and indicating that other processes must be responsible for the inward transport of the impurities. Future experiments are planned with gas throughput rates of up to 25 times larger than those used in previous experiments with the goal of reaching the so-called Rosenbluth density, above which Coulomb avalanche amplification is predicted not to occur [12].

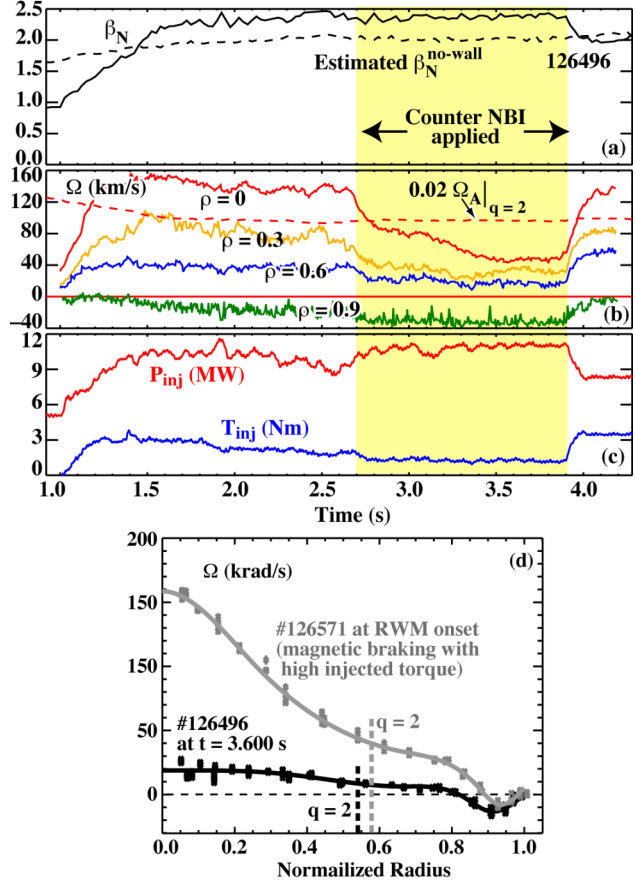


FIG. 3. (a) DIII-D discharge demonstrating sustained operation above the no-wall  $\beta$  limit ( $2.4 I_i$ ) at (b) very low rotation obtained using (c) torque control. (d) Toroidal rotation profile at RWM onset with (grey) and without magnetic braking (black).

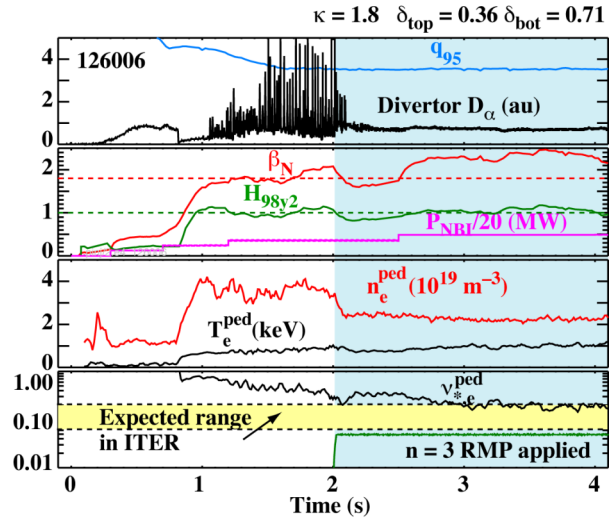


FIG. 4. Complete ELM suppression using  $n = 3$  RMP in a discharge with a shape and collisionality similar to that in ITER. The dashed lines in (b) represent the ITER  $Q = 10$  baseline target values for  $\beta_N$  (red) and  $H_{98y2}$  (green).

## 2.4. Control of Plasma Profiles

In ITER, control of the plasma density, current density, and rotation profiles will take on added importance in achieving optimal kinetic profiles due to the demonstrated dependence of transport and stability on these profiles and the inability to use external means to control the temperature profiles directly due to large self-heating. The ability to control each of these profiles has been demonstrated on DIII-D. Examples of the present capabilities with regard to rotation and current density profile control are presented in this section. Experiments demonstrating particle control capabilities are discussed as part of the scenario development highlights in Sec. 3.

**Rotation Control.** To enable tests of the importance of plasma rotation on transport and stability, the neutral beam system on DIII-D has been recently reconfigured to provide up to 5 MW of counter-NBI injected power along with 12 MW of co-NBI injected power, thereby providing a powerful tool for controlling plasma rotation. The impact of varying the applied torque on various transport and MHD quantities in stationary, moderate beta ( $\beta_N = 2.6$ ), hybrid discharges is shown in Fig. 5. As expected, the rotation velocity (and the associated rotational shear) decreases as the torque input is decreased. This strong reduction in the rotational shear is accompanied by a much weaker decrease in the thermal energy and momentum times and increases in  $\chi_i$  and  $\chi_e$ , consistent with previous studies that have shown the importance of ExB shear in radial transport. The observed anti-correlation between NTM amplitude and Mach number will likely have an impact on the overall trends in confinement and transport.

Based on this “open-loop” data, an algorithm to independently control toroidal rotation and  $\beta$  was implemented within the PCS through feedback control of both the total input power and torque input from the NBI systems. An example of the ability to independently control  $v_{\text{tor}}$  and  $\beta$  is shown in Fig. 6. The control signals utilized in this initial feedback scheme are the value of  $\beta$  from real-time equilibrium reconstructions and  $v_{\text{tor}}$  from real-time spectral analysis of charge-exchange recombination (CER) measurements.

**Current Density Profile Control.** Active control of the current density profile (or equivalently the safety factor  $q$  profile) offers many advantages for both transport improvement and increased stability limits. The capability to actively control key aspects of

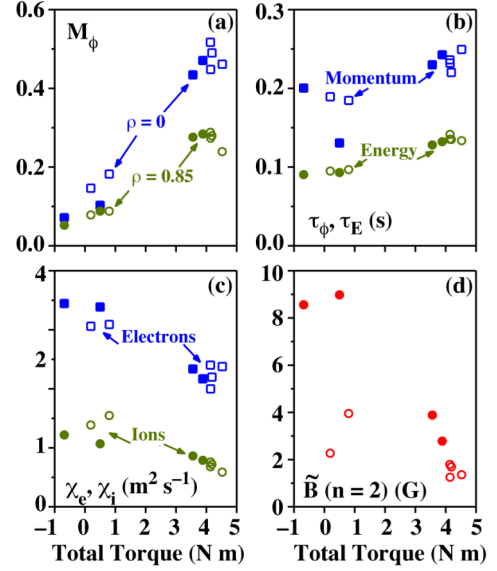


FIG. 5. Measured variation of (a) core and edge Mach number; (b) momentum and energy confinement time; (c) ion and electron thermal diffusivity at  $r/a = 0.5$ , and (d)  $m=3/n=2$  NTM amplitude with torque input in  $q_{95} = 4.5$  (open) and  $q_{95} = 4.0$  (closed) hybrid plasmas.

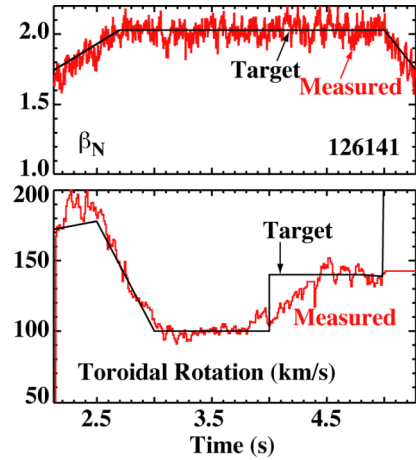


FIG. 6. Demonstration of simultaneous feedback control of  $\beta_N$  and toroidal rotation. Feedback control ends at  $t = 5.0$  s.

the  $q$  profile evolution in a regulated fashion during the target development phase of a high  $\beta$  plasma has been demonstrated in recent experiments using the DIII-D PCS [13]. This capability is illustrated in Fig. 7, which shows the measured and target values of  $q_{\min}$  in two separate cases in which NBI heating was actively controlled to maintain  $q_{\min}$  at relatively high values ( $q_{\min} > 2$ ) over a long duration ( $\sim 2$  s). To enable closed loop feedback control, the  $q$  profile is determined in real-time every 8 ms from a complete equilibrium reconstruction including internal poloidal field measurements from the motional Stark effect (MSE) diagnostic. This capability has been utilized successfully to produce the target  $q$  profile of high  $\beta$  plasmas (Fig. 9).

### 3. Advanced Scenario Development for ITER

A major long-term goal of the DIII-D research program is the development and characterization of robust advancing operating scenarios capable of becoming the new benchmark for tokamak performance, replacing the conventional, inductively driven, ELMing H-mode plasma. Towards this goal, the integration of the control techniques described in Sec. 2 has enabled an expansion of the envelope of viable, stationary tokamak operation in DIII-D, providing confidence that ITER can achieve (and potentially exceed) its basic research mission tasks and increasing the credibility of high  $\beta$ , steady-state, tokamak operation. In addition, the successful integration of these tools has allowed tests of the compatibility of these enhanced performance regimes with anticipated conditions in burning plasmas, such as low rotation,  $T_e \sim T_i$ , and high radiative power fractions.

#### 3.1. High $\beta$ , Steady-State Scenarios

The credibility of high  $\beta$ , steady-state, tokamak operation and the ability to achieve  $Q = 5$  steady-state operation in ITER has been bolstered by recent experiments in DIII-D demonstrating sustained ( $\sim 2$  s) operation with  $\beta_N \simeq 4$  (50% above the no-wall stability limit) as well as fully noninductive operation with  $\beta \simeq 3.5\%$ . The progress made in 2005-2006 is illustrated in Fig. 8 where the fusion ignition figure of merit  $G = \beta_N H_{89} / q_{95}^2$  is plotted versus the bootstrap current fraction  $f_{bs} = I_{bs} / I_p$ . In 2004, proof-of-principle, Advanced Tokamak discharges had been developed that marginally met the ITER steady-state scenario target values ( $G = 0.3$ ,  $f_{bs} = 50\%$ ) [14]. Over the past two years, higher performance discharges ( $G = 0.4$ ,  $f_{bs} = 55\%$ ) have been developed based on the successful integration of several of the

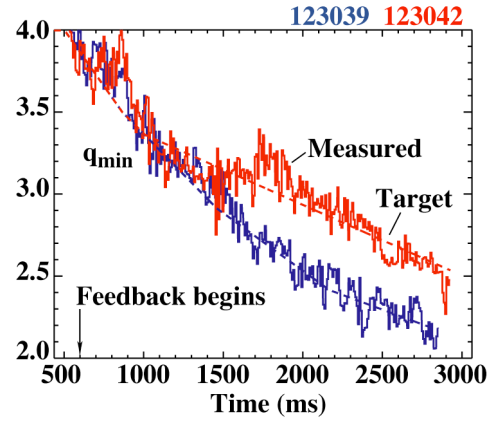


FIG. 7. Two cases demonstrating the capability to regulate the evolution of  $q_{\min}$  through feedback control of the neutral beam input power using the DIII-D PCS.

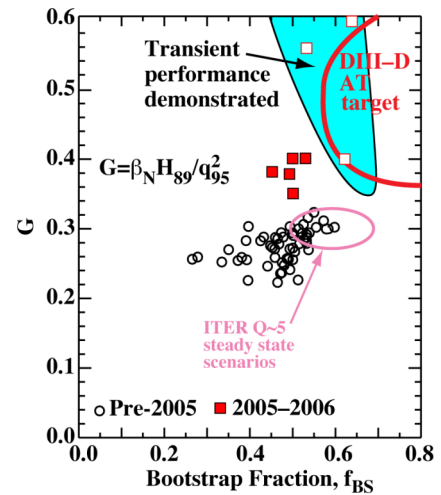


FIG. 8. Achieved values of  $G$  and  $f_{BS}$  in DIII-D discharges. The open squares in the shaded region represent discharges using  $B_T$  and  $I_p$  ramps to transiently achieve high performance while the closed squares use techniques that are in principle capable of steady-state operation. The open circles are from data prior to the 2005 experimental campaign.

aforementioned control tools (e.g., RWM stabilization, current profile control, density control). Insufficient ECCD power to maintain the current density profile during the high  $\beta$  phase has limited efforts to extend these to fully noninductive operation. Modifications to the lower divertor in DIII-D now allow balanced double-null (DN) operation with good density control (20% lower than that achieved with limited pumping capability), though the density obtained so far is 10%-20% higher than in previous upper-single-null discharges. This increase is at least partly attributable to the lower EC power, which has been shown previously to cause density reduction.

The 2005-06 data points in Fig. 8 include two separate lines of research in which the target  $q$  profiles are obtained by distinctly different means. In both cases, highly shaped (elongation  $\kappa = 1.9$ , triangularity  $\delta = 0.65$ ), balanced DN plasma shapes are utilized to maximize the attainable  $\beta$ . The first class of discharges utilizes feedback control of  $T_e$  and  $n_e$  during the target formation phase along with simultaneous ramps of  $I_p$  and  $B_T$  to produce broad current profiles with moderate, negative central shear (NCS) and  $q_{\min} > 2$  [6]. An example of this type of discharge is shown in Fig. 2. In this case,  $\beta_N \simeq 4$ , and  $H_{89} \simeq 2.5$  is sustained for  $\sim 2$  s in the presence of negative central shear and an internal transport barrier in the ion thermal channel.  $G = 0.8$ ,  $\beta_T \simeq 7\%$  and  $f_{BS} = 60\%$  are achieved transiently (due to the  $I_p$  and  $B_T$  ramps). Detailed analysis of the current profile evolution indicates that the ramps in  $I_p$  and  $B_T$  act to drive significant off-axis inductive current. Although this means of sustaining the current profile is not compatible with steady-state operation, the excellent stability and transport properties observed in this case confirm theoretical predictions of the benefits of providing off-axis current drive to produce a broad current profile with elevated  $q_{\min}$ .

In the second class of discharges [14,15], an L-H transition is induced early in the current ramp ( $\sim 400$  ms) which broadens the temperature profile and slows down the penetration of the current density, allowing the development of a current profile with weak NCS and  $q_{\min} \sim 2$  at the beginning of the high  $\beta$  phase. During the high  $\beta$  phase, ECCD is utilized to maintain this broad current profile. An example of this class of discharge is shown in Fig. 9.

In this case,  $\beta_N = 3.8$ ,  $H_{89} = 2.5$ ,  $G = 0.4$ ,  $f_{BS} = 50\%$  is sustained for over 1 s. Systematic studies have shown that the  $\beta$  limit is 10%-15% higher in DN plasma shapes compared to previously obtained results in a upper, single null plasma shape with the same  $\kappa$  and  $\delta$ . In addition, a strong dependence of the  $\beta$  limit and overall confinement on the details of the plasma shape has been observed in studies in which the outer “squareness” is varied while maintaining the same  $\kappa$  and  $\delta$  [16]. The observed sensitivity (variations of 10% in  $\beta$  limit and overall confinement) suggests the importance of shape details on performance in ITER [17] and the possibility of a hidden variable that is not accounted for in the standard confinement scalings.

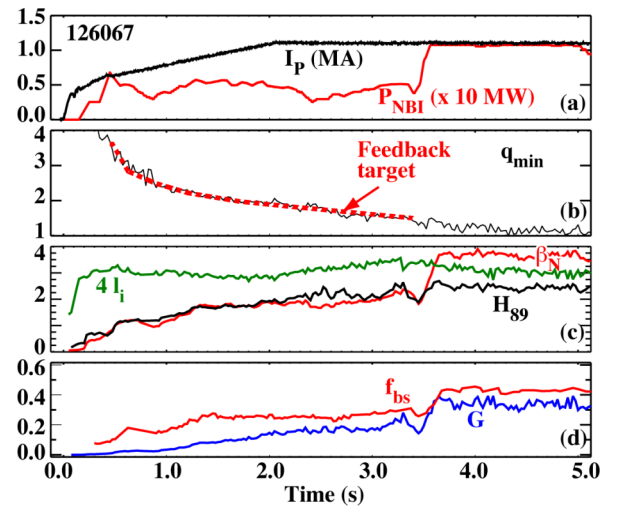


FIG. 9.  $\beta_N \simeq 3.8$ ,  $H_{89} = 2.5$ ,  $G = 0.34$  discharge in which current profile control was used to form the target  $q$  profile for the high  $\beta$  phase.

### 3.2. Hybrid Regime

Previous studies on DIII-D (performed with co-NBI only) have documented the development of stationary discharges that offer potential performance enhancements in ITER beyond its  $Q = 10$  baseline mission [18,19]. Recent experiments have extended these results to include high performance operation at low plasma rotation and with an ITER-similar shape. An example of a low-rotation, stationary discharge with  $q_{95} = 3$  with  $G = 0.47$  sustained for over 5 s (or  $\sim 5 \tau_R$ ) is shown in Fig. 10. The toroidal rotation in this case is roughly a factor of 3 lower than the rotation in previous hybrid discharges at this  $q_{95}$ . This level of performance compares to  $G = 0.6$  in co-NBI,  $q_{95} = 3$  hybrid discharges, but is still well above the normalized performance level required for  $Q = 10$  operation in ITER ( $G = 0.42$ ). A similar performance reduction is observed in  $q_{95} \sim 4.5$  discharges, but the performance ( $G = 0.32$ ) remains comparable to that needed for the ITER baseline mission. Other than the decrease in confinement, the beneficial characteristics of hybrid plasmas (sawteeth mitigation, benign NTMs, high beta operation) are retained in these low rotation cases.

In addition to low rotation operation, the space over which these improved performance conditions can be sustained has been significantly expanded recently. This expansion of the operating space has enabled a variety of studies aimed at understanding transport in this regime as well as assessing the compatibility of this regime with anticipated ITER-like conditions, such as low rotation and high radiative power fractions. The compatibility of enhanced performance plasmas with high radiative power fractions has been demonstrated using argon injection into otherwise stationary “hybrid”, USN plasmas with  $\beta_N = 2.6$ ,  $H_{89} = 2.1$ , and  $G = 0.4$  [20]. Using the “puff-and-pump” technique, high values of argon enrichment in the divertor region ( $\eta_{Ar} \sim 30$ ) are inferred from measurements of the argon concentrations in the core and pumping plenum regions. This high argon enrichment permits high radiative fractions (63%) and a factor of 2 decrease in divertor heat flux with minimal core dilution ( $f_{Ar, core} = 0.2\%$ ) and negligible impact on  $\beta_N$ ,  $H_{89}$ , or  $G$ .

### 4. Advances in Scientific Understanding

Enabled by significant advances in diagnostic capabilities and the aforementioned control tool set, the DIII-D program has advanced significantly the understanding of key processes that govern plasma performance. These advances are aimed at ultimately providing the ability to predict all aspects of fusion plasma performance, thereby providing a means to improve the efficiency and effectiveness of experiments in ITER and gaining the greatest scientific

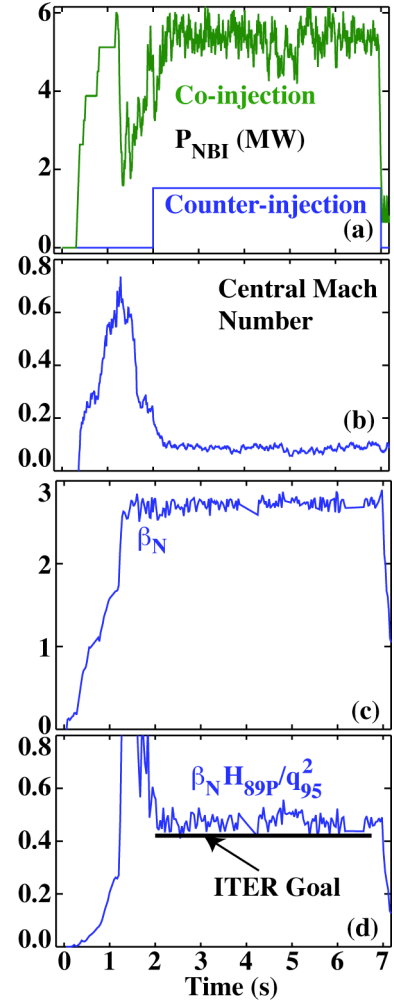


FIG. 10. Temporal evolution of a low rotation, hybrid discharge at  $q_{95} = 3.2$  with performance in excess of the requirements for  $Q = 10$  in ITER.

benefit from ITER operation. Examples of some of the key recent advances in areas important for ITER success are discussed in this section.

#### 4.1. Energetic Particles

Energetic-particle-driven instabilities could pose a significant threat to plasma facing surfaces and achieving adequate plasma performance in ITER. Hence, developing predictive models of these instabilities before ITER operates is essential for its operation and optimization. Enabled by significant advances in diagnostic capabilities on DIII-D, direct measurements of the spatial structure of toroidal Alfvén eigenmodes (TAEs) and reversed shear Alfvén eigenmodes are now routinely available. An example of the measured radial structure from spatially resolved ECE measurements of the electron temperature perturbations is shown in Fig. 11, along with a comparison of the predicted perturbation by the ideal MHD code NOVA [21]. The qualitative agreement between the theory and experiment shown in Fig. 11 is bolstered by the observation that the absolute amplitude of the measured density fluctuations from BES and reflectometry are also consistent with the NOVA calculation. The effect of these instabilities on the fast-ion distribution can also now be measured on DIII-D using the fast ion  $D_\alpha$  (FIDA) diagnostic [22]. An example is shown in Fig. 12, which shows a direct correlation between the level of Alfvén eigenmode activity and the deficit in the fast-ion density (relative to the classically predicted value). This deficit is even larger than the deficit in the measured neutron rate relative to the classically expected value [23].

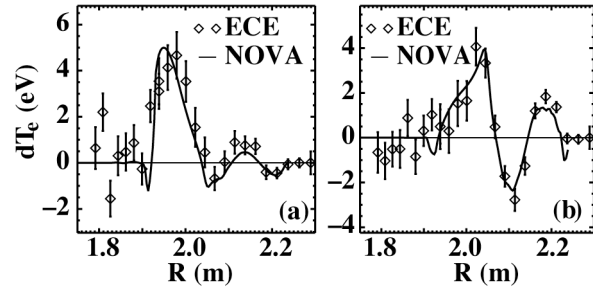


FIG. 11. Measured (symbols) and predicted (lines)  $T_e$  perturbation due to (a) RSAEs and (b) TAEs on the outboard midplane of DIII-D.

#### 4.2. Turbulence and Zonal Flow Characterization

The ability to characterize the structure and impact of turbulence in fusion plasmas has been revolutionized in recent years on DIII-D through the introduction of state-of-the-art fluctuation diagnostics, powerful computational (both analytic and predictive) tools, and new actuators for controlling transport. Recent enhancements in the DIII-D diagnostic set now provide the ability to measure turbulence characteristics over a large range in scale lengths ( $1 \text{ cm}^{-1} < k_\perp < 40 \text{ cm}^{-1}$ ). Simultaneous measurements of low  $k$  ( $0\text{--}4 \text{ cm}^{-1}$  from FIR scattering and reflectometry) and high  $k$  ( $35\text{--}40 \text{ cm}^{-1}$  from microwave backscattering) turbulence during ECH experiments have shown that while the level of high- $k$  turbulence increases with increased electron heat flux, low- $k$  turbulence levels remain virtually unchanged [24]. This unique capability has enabled detailed

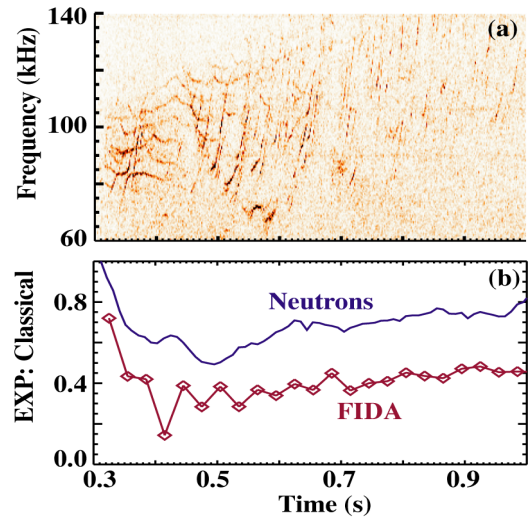


FIG. 12. Temporal evolution of (a) - Cross-power spectra between two interferometer chords; and (b) ratio of measured neutron rate and fast-ion density to their expected values assuming classically slowing down of the injected neutral beam ions.

studies of high  $k$  turbulence, characteristics of zonal flows, and the role of zonal flows near rational surfaces on the triggering of internal transport barriers.

A key insight garnered from theory and confirmed by experiment over the past few years has been the important role that zonal flows play in regulating turbulence-driven transport. Zonal flows are radially localized, poloidally and toroidally uniform ( $n = 0$ ,  $m \equiv 0$ ) electrostatic fluctuations that are excited by drift wave turbulence, removing free energy from the underlying turbulence and thereby regulating the transport process [25]. Detailed analysis of data from the upgraded DIII-D beam emission spectroscopy (BES) system has identified and characterized two classes of zonal flows – the geodesic acoustic mode (GAM) and the zero-mean-frequency (ZMF) zonal flow (Fig. 13). GAMs are localized near the plasma edge ( $0.85 < r/a < 1.0$ ). Time-delay-estimation (TDE) techniques indicate that the GAMs not only modulate the intensity of the underlying turbulence but also act to drive a transfer of internal energy from low to high frequencies, as predicted by theory [26]. The ZMF zonal flow is a low-frequency, spectrally broad ( $\Delta f \sim 10$  kHz) poloidal flow structure that peaks near zero frequency in the plasma core region ( $0.6 < r/a < 0.9$ ) [27]. Consistent with theoretical predictions, these ZMF zonal flows are characterized by a poloidal correlation length of the velocity fluctuations being significantly longer than the poloidal correlation length for density fluctuations and a radial correlation length of the poloidal velocity fluctuations ( $\sim 1$ -2 cm) comparable to the background turbulence radial correlation length.

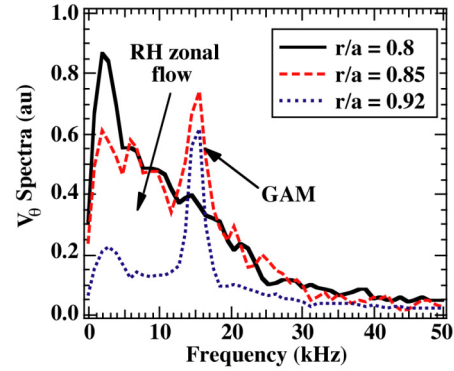


FIG. 13. Poloidal velocity fluctuation spectra at three radial locations, exhibiting a transition from a GAM dominated spectrum near the edge to the ZMF zonal flow dominated spectrum towards the core.

In addition to regulating turbulence-driven transport, DIII-D measurements coupled with GYRO simulations suggest that zonal flows play an important role in the formation of internal transport barriers near low order rational  $q$  values that has been commonly observed in NCS plasmas worldwide [28]. The emerging picture from these studies is that the scarcity of rational surfaces at low order rational  $q$  values lead to “profile corrugations” associated with time-averaged components of zonal flows near the rational surface. Provided the background ExB shear is marginal for decorrelating the underlying turbulence, the zonal-flow-induced increase in ExB shear is sufficient to cause dramatic reductions in local transport and formation of a core transport barrier. In cases without sufficient background ExB shear, transient reductions in transport are observed but do not lead to the formation of a core transport barrier.

### 4.3. Edge/Material Surface Optimization and Understanding

DIII-D is well positioned to provide the physics basis for carbon-based plasma facing materials owing to its  $\sim 95\%$  coverage of the main chamber walls with graphite tiles. A key objective is to provide the physics basis for the choice of carbon as a primary plasma facing material in ITER. To this end, recent experiments on DIII-D have documented the migration path of carbon in ELMing H-mode plasmas, demonstrated that deuterium co-deposition with carbon is dramatically reduced in heated materials, and established the capability to produce and sustain high performance plasmas on de-conditioned graphite walls.

**Carbon Transport and Deposition.** Analysis of a set of graphite tiles removed immediately following an experiment in which  $C^{13}H_4$  was injected into a reproducible set of detached, ELMing H-mode discharges shows that the largest deposition of  $C^{13}$  was localized to the inner divertor and private flux region [29]. This deposition pattern has been qualitatively reproduced in two-dimensional edge modeling using an *ad-hoc* parallel flow with a Mach number  $M \sim 0.4$  directed toward the inner divertor in conjunction with an imposed inward convection ( $V_{pinch} \sim 10$  m/s) above the divertor region. Based on measurements showing toroidal symmetry of the deposition, approximately 40% of the injected  $C^{13}$  are deposited in the lower divertor region. High sensitivity analysis indicates that small levels of  $C^{13}$  are deposited on the inner wall and regions near the aperture from the upper plenum to the main chamber. Separate studies using the DIII-D DiMES system has shown that deuterium co-deposition in simulated tile gaps is reduced by a factor of 10 when the tile gap was heated to 200°C as opposed to room temperature [30]. These results, combined with results from  $C^{13}$  transport studies suggest a possible solution to the tritium retention issue in ITER by using heating of the inner divertor substrate.

**Effect of Wall Conditioning on Performance.** Finally, a recent set of experiments in DIII-D has demonstrated the ability to access and sustain high performance plasmas without routine boronization. In these experiments, performance levels achieved in Advanced Tokamak and hybrid discharges soon after boronization were duplicated in discharges taken over 6000 s of plasma operation after boronization. The temporal evolution of four AT discharges taken at various times during the 2006 experiment campaign is shown in Fig. 14. Except for the duration of the high performance phase, these discharges are nearly identical in all respects. In each case shown, the normalized performance is among the highest ever achieved in an AT discharge, indicating the ability to produce high performance discharges over an extended period without boron-conditioning of the graphite tiles. A separate experiment with the graphite wall in its “unboronized” state also demonstrated the ability to produce seven identical, long-pulse ( $\tau_{dur} > 2 \tau_R$ ), moderate performance ( $\beta_N \sim 2.6$ ,  $H_{89} \sim 2.4$ ,  $G = 0.38$ ) hybrid discharges with strong divertor pumping yet without any between-shot wall conditioning, including helium glow cleaning. These results suggests that graphite wall conditions adequate to obtain high performance plasmas can be maintained over an extended period without conditioning provided sufficient particle exhaust is available to maintain good particle balance on a shot-to-shot basis. This is in marked contrast to recent results from Alcator C-Mod [31] in which routine conditioning of high-Z walls is required to access high performance regimes.

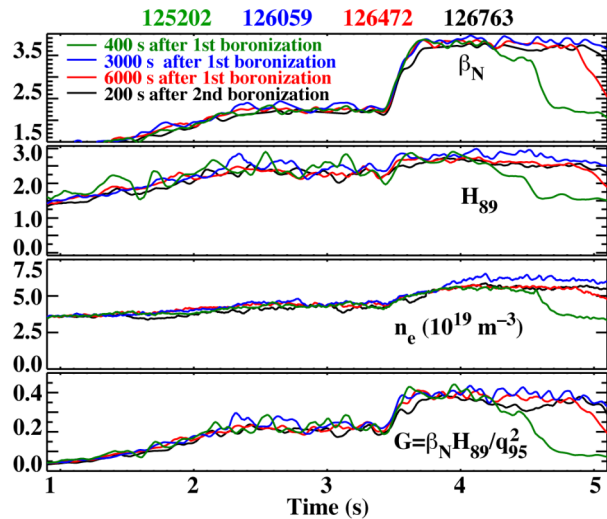


FIG. 14. Temporal evolution of four Advanced Tokamak discharges taken at various times relative to boronization of the vessel, showing remarkably similar performance characteristics in stability and confinement.

## 5. Summary

As demonstrated by the results presented above, the DIII-D research program has made significant progress in the development of physics solutions to key issues facing ITER, in demonstrating the promise of advanced operating regimes for ITER, and in providing key insights into basic fusion plasma processes. Through this research and development, the DIII-D research program has provided additional confidence that ITER can achieve its basic research mission tasks and established the physics basis for a potentially enhanced experimental program on ITER extending well beyond its baseline mission (i.e., the potential of  $Q > 10$  operation). Future research on DIII-D will focus on providing the physics basis for key ITER design issues (especially with respect to the control tool set), continued development and qualification of advanced operating regimes, and developing the scientific basis sufficiently well that the greatest scientific benefit can be obtained from ITER operation.

## Acknowledgment

This work was supported by the U.S. Department of Energy under DE-FC02-04ER54698.

## References

- [1] AYMAR, R., *et al.*, Plasma Phys. Control. Fusion **44** (2002). 519
- [2] PETTY, C.C., *et al.*, Nucl. Fusion **44** (2004) 243.
- [3] HUMPHREYS, D.A., *et al.*, Phys. Plasmas **13** (2006) 056113.
- [4] GAROFALO, A.M., *et al.*, Phys. Rev. Lett. **89** (2002) 235001-1.
- [5] STRAIT, E.J., *et al.*, Phys. Plasmas **11** (2004) 2505.
- [6] GAROFALO, A.M., *et al.*, Phys. Plasmas **13** (2006) 056110.
- [7] EVANS, T.E., *et al.*, Phys. Rev. Lett. **92** (2004) 235003.
- [8] EVANS, T.E., *et al.*, Nature Physics **2** (2006) 419.
- [9] MOYER, R.A., *et al.*, this conference.
- [10] WHYTE, D.G., *et al.*, Phys. Rev. Lett. **89** (2002) 055001-1.
- [11] HOLLMANN, E.M., Nucl. Fusion **45** (2005) 1046.
- [12] ROSENBLUTH, M.N., and PUTVINSKI, S.V., Nucl. Fusion **37** (1997) 1355.
- [13] FERRON, J.R., *et al.*, Nucl. Fusion **46** (2006) L13.
- [14] MURAKAMI, M., *et al.*, Nucl. Fusion **45** (2005) 1419.
- [15] WADE, M.R., *et al.*, Nucl. Fusion **43** (2003) 634.
- [16] GREENFIELD, C.M., *et al.*, this conference.
- [17] LEONARD, A.W., *et al.*, this conference.
- [18] WADE, M.R., *et al.*, Nucl. Fusion **45** (2005) 407.
- [19] LUCE, T.C., *et al.*, Nucl. Fusion **43** (2003) 321.
- [20] PETRIE, T.W., *et al.*, this conference.
- [19] VAN ZEELAND, M.A., *et al.*, Phys. Rev. Lett. **97** (2006) 135001.
- [21] HEIDBRINK, W.W., *et al.*, Plasma Phys. Control. Fusion **46** (2004) 1855.
- [22] HEIDBRINK, W.W., *et al.*, this conference.
- [23] RHODES, T.L., *et al.*, this conference.
- [24] DIAMOND, P., *et al.*, Plasma Phys. Control. Fusion **47** (2005) R35.
- [25] HOLLAND, C., *et al.*, "Measurement of nonlinear interactions between geodesic acoustic modes and edge turbulence in the DIII-D tokamak," submitted to Phys. Rev. Lett. (2006).
- [26] GUPTA, D.K., *et al.*, "Detection of zero-mean-frequency zonal flows in the core of a high temperature tokamak plasma," to be published in Phys. Rev. Lett. (2006).
- [27] AUSTIN, M.E., *et al.*, Phys. Plasmas **13** (2006) 082502.
- [28] WAMPLER, W., *et al.*, "Transport and deposition of  $^{13}\text{C}$  from methane injection into partially detached divertor H-mode plasmas in DIII-D," J. Nucl. Mater., to be published (2006).
- [29] KRIEGER, K., *et al.*, "Formation of deuterium-carbon inventories in gaps of plasma facing components," J. Nucl. Mater., accepted for publication (2006).
- [30] LIPSCHULTZ, B., *et al.*, Phys. Plasmas **13** (2006) 056117.

## APPENDIX: THE DIII-D TEAM

G. Abela,<sup>1</sup> S.L. Allen,<sup>2</sup> P.M. Anderson,<sup>1</sup> R. Andre,<sup>3</sup> G. Antar,<sup>4</sup> M.E. Austin,<sup>5</sup> F.W. Baity,<sup>6</sup> J.P. Bakalarski,<sup>1</sup> D.R. Baker,<sup>1</sup> M. Bakhtiari,<sup>7</sup> D.E. Baldwin,<sup>1</sup> D.E.G. Barber,<sup>6</sup> V. Basiuk,<sup>8</sup> R. Bastasz,<sup>9</sup> C.B. Baxi,<sup>1</sup> L.R. Baylor,<sup>6</sup> M. Becoulet,<sup>8</sup> E.A. Belli,<sup>1</sup> H.L. Berk,<sup>5</sup> J.M. Bialek,<sup>10</sup> J. Blair,<sup>11</sup> J.A. Boedo,<sup>4</sup> I.N. Bogatu,<sup>12</sup> R.L. Boivin,<sup>1</sup> R.V. Bravenec,<sup>5</sup> B.D. Bray,<sup>1</sup> D.P. Brennan,<sup>13</sup> S. Brezinsek,<sup>14</sup> N.H. Brooks,<sup>1</sup> R.V. Budny,<sup>3</sup> K.H. Burrell,<sup>1</sup> R.J. Buttery,<sup>15</sup> O. Buzhinskij,<sup>16</sup> J.D. Callen,<sup>7</sup> R.W. Callis,<sup>1</sup> G.L. Campbell,<sup>1</sup> J.M. Candy,<sup>1</sup> T.N. Carlstrom,<sup>1</sup> W.P. Cary,<sup>1</sup> T.A. Casper,<sup>2</sup> V.S. Chan,<sup>1</sup> M.S. Chance,<sup>3</sup> E. Chin,<sup>1</sup> H.K. Chiu,<sup>1</sup> M. Choi,<sup>1</sup> M.S. Chu,<sup>1</sup> S. Cirant,<sup>17</sup> R.J. Colchin,<sup>6</sup> S.K. Combs,<sup>6</sup> J. Culver,<sup>18</sup> J.W. Davis,<sup>18</sup> W. Davis,<sup>3</sup> J.S. deGrassie,<sup>1</sup> J.C. DeBoo,<sup>1</sup> J.L. Doane,<sup>1</sup> R.P. Doerner,<sup>4</sup> V. Dokouka,<sup>16</sup> J. Dorris,<sup>13</sup> E.J. Doyle,<sup>19</sup> F. Dubois,<sup>8</sup> D.H. Edgell,<sup>20</sup> D. Elder,<sup>18</sup> R.A. Ellis, III,<sup>3</sup> R.F. Ellis,<sup>21</sup> C. Estrada-Mila,<sup>4</sup> T.E. Evans,<sup>1</sup> E. Feibush,<sup>3</sup> M.E. Fenstermacher,<sup>2</sup> J.R. Ferron,<sup>1</sup> K.H. Finken,<sup>14</sup> D.K. Finkenthal,<sup>22</sup> R.K. Fisher,<sup>1</sup> S.M. Flanagan,<sup>1</sup> R.J. Fonck,<sup>7</sup> C-M. Fransson,<sup>23</sup> E. Fredd,<sup>3</sup> E.D. Fredrickson,<sup>3</sup> S.A. Galkin,<sup>24</sup> Q. Gao,<sup>25</sup> A.M. Garofalo,<sup>10</sup> K.W. Gentle,<sup>5</sup> R. Gianella,<sup>8</sup> M. Gilmore,<sup>26</sup> P. Gohil,<sup>1</sup> X. Gong,<sup>25</sup> I.A. Gorelov,<sup>1</sup> R.H. Goulding,<sup>6</sup> M.T. Green,<sup>1</sup> K.L. Greene,<sup>1</sup> C.M. Greenfield,<sup>1</sup> N.L. Greenough,<sup>3</sup> R.J. Groebner,<sup>1</sup> M. Groth,<sup>2</sup> H.J. Grunloh,<sup>1</sup> M. Graznevitch,<sup>15</sup> S. Günter,<sup>27</sup> D. Gupta,<sup>7</sup> K. Halletschek,<sup>27</sup> M.J. Hansink,<sup>1</sup> R.J. Harrington,<sup>27</sup> J.H. Harris,<sup>29</sup> S. Harrison,<sup>7</sup> R.W. Harvey,<sup>30</sup> R. Hatcher,<sup>3</sup> N.C. Hawkes,<sup>15</sup> C.C. Hegna,<sup>7</sup> W.W. Heidbrink,<sup>31</sup> T.C. Hender,<sup>15</sup> F.L. Hinton,<sup>1</sup> J.T. Hogan,<sup>6</sup> C. Holcomb,<sup>2</sup> C. Holland,<sup>4</sup> E.M. Hollman,<sup>4</sup> K.L. Holtrop,<sup>1</sup> R.-M. Hong,<sup>1</sup> J.C. Hosea,<sup>3</sup> N. Howard,<sup>32</sup> D.F. Howell,<sup>15</sup> W.A. Houlberg,<sup>6</sup> C.-L. Hsieh,<sup>1</sup> C. Hu,<sup>25</sup> D.A. Humphreys,<sup>1</sup> P. Huynh,<sup>1</sup> A.W. Hyatt,<sup>1</sup> F. Imbeaux,<sup>8</sup> Y. In,<sup>12</sup> K. Indreshkumar,<sup>5</sup> A. Isayama,<sup>33</sup> R.C. Isler,<sup>6</sup> G.L. Jackson,<sup>1</sup> A.M. Jacques,<sup>1</sup> M. Jakabowski,<sup>14</sup> A.N. James,<sup>4</sup> S.C. Jardin,<sup>3</sup> R.J. Jayakumar,<sup>2</sup> T.C. Jernigan,<sup>6</sup> H. Jhang,<sup>34</sup> E.H. Joffrin,<sup>8</sup> R.D. Johnson,<sup>1</sup> I. Joseph,<sup>4</sup> K. Kajiwara,<sup>35</sup> D.H. Kaplan,<sup>1</sup> S. Kasilo,<sup>36</sup> O. Katsuro-Hopkins,<sup>10</sup> J.-Y. Kim,<sup>25</sup> K.M. Keith,<sup>1</sup> A.G. Kellman,<sup>1</sup> D.H. Kellman,<sup>1</sup> M.A.H. Kempnaars,<sup>37</sup> C. Kessel,<sup>3</sup> R. Khayrutdinov,<sup>16</sup> C. Kim,<sup>7</sup> J.S. Kim,<sup>12</sup> L. Kim,<sup>1</sup> J.E. Kinsey,<sup>11</sup> W.-H. Ko,<sup>34</sup> G.J. Kramer,<sup>3</sup> S.I. Krasheninnikov,<sup>4</sup> K. Krieger,<sup>27</sup> S.E. Kruger,<sup>38</sup> R.J. La Haye,<sup>1</sup> L.L. Lao,<sup>1</sup> C.J. Lasnier,<sup>2</sup> E.A. Lazarus,<sup>6</sup> J.-N. Leboeuf,<sup>19</sup> R.L. Lee,<sup>1</sup> H. Lee,<sup>34</sup> X. Lee,<sup>1</sup> M. Lehnen,<sup>14</sup> A.W. Leonard,<sup>1</sup> J.A. Leuer,<sup>1</sup> Y.R. Lin-Liu,<sup>39</sup> S. Lisgo,<sup>18</sup> A. Litnovsky,<sup>14</sup> C. Liu,<sup>1</sup> Y.Q. Liu,<sup>40</sup> A. Loarte,<sup>27</sup> J. Lohr,<sup>1</sup> J. Lonroth,<sup>41</sup> T.C. Luce,<sup>1</sup> C. Ludescher-Furth,<sup>3</sup> Y. Luo,<sup>31</sup> J.L. Luxon,<sup>1</sup> M.A. Mahdavi,<sup>1</sup> J. Mailloux,<sup>15</sup> R. Maingi,<sup>6</sup> C.C. Makariou,<sup>1</sup> M.A. Makowski,<sup>2</sup> J. Manickam,<sup>3</sup> A. Manini,<sup>27</sup> M.E. Maraschek,<sup>27</sup> G. Matsunaga,<sup>33</sup> P.S. Mauzey,<sup>1</sup> D. Mazon,<sup>8</sup> D.C. McCune,<sup>3</sup> B.B. McHarg,<sup>1</sup> G.R. McKee,<sup>7</sup> A.G. McLean,<sup>18</sup> J.E. Menard,<sup>3</sup> W.H. Meyer,<sup>2</sup> D. Mikkelsen,<sup>3</sup> C.P. Moeller,<sup>1</sup> J.M. Moller,<sup>2</sup> P. Monier-Garbet,<sup>8</sup> R.A. Moyer,<sup>4</sup> A. Mui,<sup>22</sup> M. Murakami,<sup>6</sup> C.J. Murphy,<sup>1</sup> A. Nagy,<sup>3</sup> E. Nardon,<sup>8</sup> M.F.A. Nave,<sup>42</sup> G.A. Navratil,<sup>10</sup> R. Nazikian,<sup>3</sup> A. Nerem,<sup>1</sup> X.V. Nguyen,<sup>19</sup> H. Nishino,<sup>43</sup> S. Noraky,<sup>1</sup> T. Oikawa,<sup>33</sup> M. Okabayashi,<sup>3</sup> R.A. Olstad,<sup>1</sup> T.H. Osborne,<sup>1</sup> L.W. Owens,<sup>6</sup> Y. Ou,<sup>11</sup> N.A. Pablant,<sup>4</sup> V. Parail,<sup>44</sup> J.-M. Park,<sup>34</sup> Y.-S. Park,<sup>45</sup> C.T. Parker,<sup>1</sup> P.B. Parks,<sup>1</sup> C.J. Pawley,<sup>1</sup> J.J. Peavy,<sup>1</sup> W.A. Peebles,<sup>19</sup> B.G. Penaflo,<sup>1</sup> Q. Peng,<sup>1</sup> F.W. Perkins,<sup>3</sup> P.I. Petersen,<sup>1</sup> T.W. Petrie,<sup>1</sup> C.C. Petty,<sup>1</sup> N.Q. Pham,<sup>1</sup> J.C. Phillips,<sup>1</sup> V. Phillips,<sup>14</sup> S.D. Pinches,<sup>27</sup> A.Yu. Pigarov,<sup>4</sup> D.A. Piglowski,<sup>1</sup> R.I. Pinsker,<sup>1</sup> P.A. Politzer,<sup>1</sup> D. Ponce,<sup>1</sup> D.M. Ponce,<sup>35</sup> M. Porkolab,<sup>13</sup> G.D. Porter,<sup>2</sup> R. Prater,<sup>1</sup> D.G. Pretty,<sup>29</sup> L.E. Randerson,<sup>3</sup> D.A. Rasmussen,<sup>6</sup> H. Reimerdes,<sup>10</sup> E.E. Reis, Jr.,<sup>1</sup> M.E. Rensink,<sup>2</sup> T.L. Rhodes,<sup>19</sup> T.D. Rognlien,<sup>2</sup> L. Roquemore,<sup>3</sup> D.W. Ross,<sup>5</sup> J.C. Rost,<sup>13</sup> D.L. Rudakov,<sup>4</sup> A. Runov,<sup>46</sup> E. Ruskov,<sup>31</sup> F. Ryter,<sup>27</sup> Y. Sakamoto,<sup>33</sup> G. Saibene,<sup>27</sup> O. Sauter,<sup>47</sup> R.I. Savercool,<sup>1</sup> M.J. Schaffer,<sup>1</sup> D.P. Schissel,<sup>1</sup> D.J. Schlossberg,<sup>7</sup> R. Schneider,<sup>46</sup> E. Schuster,<sup>11</sup> O. Schmitz,<sup>14</sup> D.D. Schnack,<sup>48</sup> M. Schneider,<sup>8</sup> E. Schuster,<sup>11</sup> J.T. Scoville,<sup>1</sup> D. Sellers,<sup>1</sup> M.W. Shafer,<sup>7</sup> A. Shaw,<sup>1</sup> B. Shen,<sup>25</sup> K.C. Shoolbred,<sup>1</sup> A.C.C. Sips,<sup>27</sup> L. Schmitz,<sup>19</sup> A.P. Smirnov,<sup>49</sup> P.B. Snyder,<sup>1</sup> E.R. Solano,<sup>50</sup> W.M. Solomon,<sup>3</sup> H.E. St John,<sup>1</sup> W.M. Stacey,<sup>51</sup> G.M. Staebler,<sup>1</sup> R.D. Stambaugh,<sup>1</sup> P.C. Stangeby,<sup>18</sup> R. Stempork,<sup>1</sup> E.J. Strait,<sup>1</sup> D. Szymanski,<sup>1</sup> H. Takahashi,<sup>3</sup> M. Takechi,<sup>33</sup> P.L. Taylor,<sup>1</sup> T.S. Taylor,<sup>1</sup> R.J. Temkin,<sup>13</sup> T.B. Terpstra,<sup>1</sup> D.M. Thomas,<sup>1</sup> P.R. Thomas,<sup>8</sup> J.F. Tooker,<sup>1</sup> A.D. Turnbull,<sup>1</sup> G.R. Tynan,<sup>4</sup> M.A. Ulrickson,<sup>9</sup> B. Unterberg,<sup>14</sup> H. Urano,<sup>33</sup> M.A. VanZeeland,<sup>35</sup> S. Visser,<sup>1</sup> F. Volpe,<sup>52</sup> M.R. Wade,<sup>1</sup> F.L. Waelbroeck,<sup>5</sup> R. Wagner,<sup>4</sup> M.L. Walker,<sup>1</sup> R.E. Waltz,<sup>1</sup> W.R. Wampler,<sup>9</sup> B. Wan,<sup>53</sup> A. Wang,<sup>25</sup> G. Wang,<sup>19</sup> H. Wang,<sup>25</sup> J.G. Watkins,<sup>9</sup> G.W. Watson,<sup>31</sup> A.S. Welander,<sup>1</sup> J.C. Wesley,<sup>1</sup> W.P. West,<sup>1</sup> J. Whaley,<sup>9</sup> A.E. White,<sup>19</sup> D.G. Whyte,<sup>13</sup> H.R. Wilson,<sup>15</sup> S. Wolfe,<sup>3</sup> C.P.C. Wong,<sup>1</sup> K.-L. Wong,<sup>3</sup> S.K. Wong,<sup>1</sup> L. Yan,<sup>25</sup> L. Yang,<sup>25</sup> H.H. Yip,<sup>1</sup> J. Yu,<sup>4</sup> L. Zeng,<sup>19</sup> C. Zhang,<sup>53</sup> D. Zhou,<sup>53</sup> Y. Zhu<sup>31</sup>

- <sup>1</sup>General Atomics
- <sup>2</sup>Lawrence Livermore National Laboratory
- <sup>3</sup>Princeton Plasma Physics Laboratory
- <sup>4</sup>University of California, San Diego
- <sup>5</sup>University of Texas at Austin
- <sup>6</sup>Oak Ridge National Laboratory
- <sup>7</sup>University of Wisconsin, Madison
- <sup>8</sup>CEA Cadarache Euratom Association
- <sup>9</sup>Sandia National Laboratories
- <sup>10</sup>Columbia University
- <sup>11</sup>Lehigh University
- <sup>12</sup>FARTECH, Inc.
- <sup>13</sup>Massachusetts Institute of Technology
- <sup>14</sup>FZ-Julich Euratom Association
- <sup>15</sup>UKAEA Fusion Culham Science Center
- <sup>16</sup>Troitsk Institute of Innovative & Thermonuclear Investigations
- <sup>17</sup>INEA, Frascati
- <sup>18</sup>University of Toronto
- <sup>19</sup>University of California, Los Angeles
- <sup>20</sup>LLE, University of Rochester
- <sup>21</sup>University of Maryland
- <sup>22</sup>Palomar Community College
- <sup>23</sup>Tomlab Optimization Inc.
- <sup>24</sup>Keldysh Institute
- <sup>25</sup>SWIPP, Chengdu, China
- <sup>26</sup>U. New Mexico
- <sup>27</sup>Max Planck Institut für Plasmaphysik
- <sup>28</sup>Rensselaer Polytechnic Institute
- <sup>29</sup>Australian National University
- <sup>30</sup>CompX
- <sup>31</sup>University of California, Irvine
- <sup>32</sup>University of Illinois
- <sup>33</sup>Japan Atomic Energy Agency (JAEA)
- <sup>34</sup>National Fusion Research Center, Korea
- <sup>35</sup>Oak Ridge Institute of Science Education
- <sup>36</sup>Kharkov Institute for Physics & Technology
- <sup>37</sup>FOM-Rijnhuizen
- <sup>38</sup>Tech-X
- <sup>39</sup>Dong Hua University
- <sup>40</sup>Chalmers University
- <sup>41</sup>Helsinki University, Finland
- <sup>42</sup>EURATOM/IST, Lisbon
- <sup>43</sup>Hiroshima University, Japan
- <sup>44</sup>Culham, UKAEA
- <sup>45</sup>Seoul University, Korea
- <sup>46</sup>Max Planck Institute, Griefswald
- <sup>47</sup>CRPP-EPFL, Lausanne
- <sup>48</sup>SAIC
- <sup>49</sup>Moscow State University
- <sup>50</sup>EURATOM/CIEMET, Madrid
- <sup>51</sup>Georgia Institute of Technology
- <sup>52</sup>Max-Planck, Gesellschaft
- <sup>53</sup>ASIPP, Hefei